Direct observation of the momentum distribution and renormalization factor in lithium

N. Hiraoka,[1,*] Y. Yang,[2] T. Hagiya,[3] A. Niozu,[3] K. Matsuda,[3] S. Huotari,[4] M. Holzmann,[5] and D. M. Ceperley[2]

[1]*National Synchrotron Radiation Research Center, Hsinchu 30076, Taiwan*
[2]*Department of Physics, University of Illinois, Urbana, Illinois 61801, USA*
[3]*Graduate School of Science, Kyoto University, Kyoto 606-8502, Japan*
[4]*Department of Physics, POB 64, FI-00014, University of Helsinki, Helsinki, Finland*
[5]*Univ. Grenoble Alpes, CNRS, LPMMC, 38000 Grenoble, France*

(Received 30 December 2019; accepted 25 March 2020; published 20 April 2020)

We have measured the momentum distribution and renormalization factor Z_{k_F} in liquid and solid lithium by high-resolution Compton scattering. High-resolution data over a wide momentum range exhibit a clear feature of the renormalization and a sharp drop of momentum densities at the Fermi momentum k_F. These results are compared with those computed by quantum Monte Carlo simulation performed both on a disordered crystal and a liquid exhibiting very good agreement. Asymptotic behavior of the experimental and theoretical momentum distributions are examined to estimate Z_{k_F}. The experimentally obtained $Z_{k_F} = 0.43^{+0.11}_{-0.01}$ for liquid Li and $0.54^{+0.11}_{-0.02}$ for solid Li are in good agreement with theoretical results of 0.54 ± 0.01 and 0.64 ± 0.01, respectively.

DOI: 10.1103/PhysRevB.101.165124

I. INTRODUCTION

A free Fermi gas has fully occupied momentum states below the Fermi surface and unoccupied ones above. However, the electrons in an actual metal have a continuous occupation number between zero and one for all values of momentum because electron-electron interactions causes electrons to be scattered from below the Fermi surface to above the Fermi surface [1–3]. This reduces the discontinuity of the occupation number at the Fermi surface though it still exists; the remaining discontinuity is proportional to the renormalization factor Z_{k_F} [4,5]. The electron-ion interaction leads to secondary Fermi surfaces in higher Brillouin zones, so the discontinuity can be further reduced but still remains. The renormalization factor may be considered as a quantity that defines how correlated electrons are in a given material. For example, in strongly correlated systems such as heavy fermion meterials, a substantially reduced Z_{k_F} (or similar features) is reported [6–8]. Nonetheless, there is very little opportunity to directly measure the momentum distribution since very few experimental techniques allow us to estimate the Z_{k_F} in a quantitative manner. In fact, even for the simplest metals like Li and Na, an exact agreement has not been achieved between experiment and theory so far.

The energy spectrum of Compton-scattered photons provides information on the electron momentum density (EMDs) [9]. Under the impulse approximation [10,11], the differential scattering cross-section is proportional to the Compton profile (CP), defined as

$$\frac{d^2\sigma}{d\Omega dE} \propto J(p_z) = \int\int n(k_x, k_y, k_z = p_z)\, dk_x dk_y. \qquad (1)$$

Because of energy and momentum conservation, p_z can be determined from the scattered photon energy E once the incident photon energy E_o and the scattering angle θ are given. To determine the momentum density $n(\mathbf{k})$, a tomographic reconstruction is generally necessary from the CPs measured in various directions. For an isotropic sample, $n(\mathbf{k})$ can be obtained from the derivative

$$n(k) = -\frac{1}{2\pi p}\frac{dJ(p)}{dp}\bigg|_{p=k}. \qquad (2)$$

Note that $n(k)$ obtained in this way has very large errors at small values of k because of the small phase space there. An advantage of Compton scattering is that a sum rule is available so the CP can be normalized by the known electron density, allowing an absolute quantitative comparison between theory and experiment. Though the observation of $n(k)$ and Z_{k_F} is straightforward in principle, reports of direct measurements are extremely rare because the resolution of the experiments is usually not high enough. To our knowledge, a report on Na a decade ago is the only successful example [12]. Even in this case, $n(k)$ was only shown in a limited region near k_F, not permitting comparison of the overall shape of $n(k)$.

Lithium has been investigated as a case in which the homogeneous electron gas (HEG) model is applicable. However, there has been discrepancy for several decades. Interacting HEG models generally predict Z_{k_F} in the range 0.6–0.7 at Li valence density $r_s = 3.25$. The first experimental determination performed by Schülke *et al.* provided 0.1 ± 0.1 along the [100] axis based on a model analysis on $n(k)$ obtained *via* a reconstruction on a single crystal [13]. In fact, there is a tendency for theory to predict higher CPs in $p < p_F$ while lower in $p > p_F$ [14]. Kubo [15,16] ascribed this to electron correlation effects, showing that his GW calculation agreed well with experiments and had a lower Z_{k_F}. He

*hiraoka@spring8.or.jp

found a variation in Z_{k_F} between 0.15–0.35 along several crystallographic axes. Filippi and Ceperley calculated CPs by quantum Monte Carlo (QMC) simulation that explicitly included electron-ion and electron-electron interactions, and concluded that electron correlation only partly accounted for the difference between theory and experiment [17]. Disorder [18] and temperature [19] were discussed as contributing to the difference but their analysis was not conclusive, leaving the puzzle unsolved. Recently, Klevak *et al.* [20] calculated EMD by a real-space multiple-scattering Green's function approach including disorder and found a smooth drop of $n(k)$ at k_F without a finite Z_{k_F}. We note that the conduction electrons in Li have a strong electron-ion interaction. This renders the Fermi surface anisotropic and generates secondary Fermi surfaces in higher Brillouin zones due to the *umklapp* process. This fact makes quantitative comparisons between theory and experiment difficult. This is probably the source for the discrepancy existing for several decades even though Li is one of the simplest elements.

In this paper, we estimate Z_{k_F} in Li using ultrahigh-resolution Compton scattering. A 0.016 atomic unit (a.u.) instrumental resolution and a 0.024 a.u. overall resolution were achieved. A tomographic reconstruction of the EMD is required for solid Li because it has an anisotropic Fermi surface. However, this reconstruction produces artifacts, making a quantitative analysis difficult. To avoid this procedure, we measured Li above the melting point. The liquid sample is isotropic and thus a straightforward estimation of $n(k)$ is possible from Eq. (2). As a reference, we also measured a polycrystalline sample before melting the sample. Both samples exhibit a clear break of $n(k)$ at k_F allowing determination of the renormalization and the generic behavior of the momentum distribution of the HEG [4].

II. EXPERIMENT AND THEORY

The experiment was performed at Taiwan IXS beamline at SPring-8 (BL12XU). The most critical parameter in determining Z_{k_F} is the momentum resolution. Since a typical radius of the Fermi sphere is 0.5–1.0 a.u., a resolution of an order of 0.01 a.u. is needed to estimate Z_{k_F}, which is a technical challenge. One can easily improve the instrumental resolution if low-energy photons are used but the spectrum is then substantially broadened by final-state effects [21,22]. We have chosen $E_o = 25.54$ keV to obtain $dE = 5$ eV (instrumental), corresponding to $dp = 0.016$ a.u.

Synchrotron radiation from the undulator light source was monochromatized at 25.54 keV by Si 111 double crystals. Then the beam was focused into a $80 \times 120\,\mu m^2$ ($V \times H$) spot on the sample by a Pt toroidal mirror. The energy spectrum of the scattered photons were measured by a bent Laue spectrometer [23]. The analyzer was a 170-mm long, 80-mm wide (base), and 0.5-mm thick triangular Si crystal having a 1.27-m bending radius. The 660 reflection was used. The detector was a NaI scintillator equipped with a 8×16 channel photomultiplier tube. A 6×6 mm^2 pixel size makes an uncertainty of the scattering angle, affecting the momentum resolution in the experiment. Nonetheless, this effect only contributes to an additional broadening as small as 0.001 a.u. in the present setup.

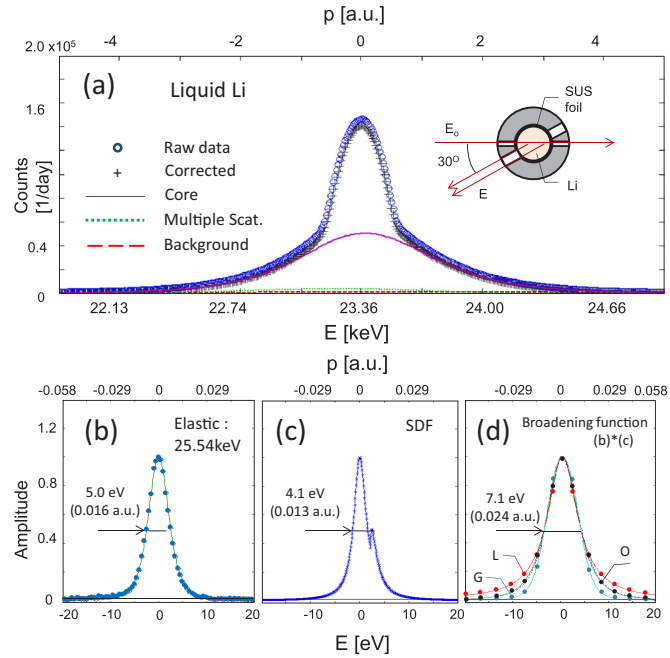

FIG. 1. (a) CPs for liquid Li. The inset shows the geometry of the experiment. (b) Elastic line, monitoring the instrumental resolution, (c) spectral density function, indicating the final-state broadening, (d) convolution of (b) and (c), providing the broadening function for a comparison with theory. O is the optimally fitted function while G and L denote Gaussian and Lorentzian, respectively.

A 99.9% purity polycrystalline Li sample having a cylindrical shape of 9-mm diameter and 10-mm height was placed in a furnace made of stainless steel (SUS) equipped with a heater at the bottom [see, Fig. 1(a), inset]. The experiment was first performed at 297 K on solid Li and then at 493 K on liquid Li. The furnace had openings along the directions of the incident and the scattered photons. To avoid the sample leaking out of the openings on the furnace when melted, the Li cylinder was first surrounded by a 10-μm-thick SUS foil in a glovebox and then it was placed in the furnace. As seen in the figure, the scattered photons from the foil were blocked by the thick part of the furnace so they were not detected.

The obtained CPs were corrected for self-absorption, background, multiple scattering, and the energy dependence of the detection system [Fig. 1(a)]. The background curve was determined by an E scan with a 2° offset of the analyzer angle. In such a geometry, the detector does not accept photons reflected from the analyzer due to Soller slits in front. Multiple scattering events were simulated up to the triple scattering process on a polycrystalline Li cylinder for the correction [24]. The energy dependence of the detection system is determined by the absorption coefficients of the sample, the air path, the analyzer, and the detector material (scintillator). Also, the reflectivity of the analyzer crystal smoothly varies as a function of the energy. Both effects were theoretically calculated and applied to the correction.

Diffusion Monte Carlo calculations were performed on molecular dynamics (MD) configurations of the ions sampled at 330 K and 500 K for the solid and the liquid phases, respectively. The classical MD temperatures were elevated

by 33 K in the solid and 7 K in the liquid phase to account for quantum fluctuations of the nuclei by matching kinetic energy following Ref. [25]. We used the Slater-Jastrow wave function with local density approximation (LDA) orbitals on simulation cells containing 432 lithium atoms. The finite-size error of the momentum distribution was corrected using the leading-order correction from Ref. [26]. The pseudopotential error was corrected using an all-electron calculation for the perfect crystal. All calculations were performed at $r_s = 3.25$. After the QMC calculation, we rescaled k and $n(k)$ to the k_Fs corresponding to the actual experimental densities ($r_s = 3.265$ for the solid and $r_s = 3.31$ for the liquid). We used LAMMPS [27] for the MD simulations, QUANTUM ESPRESSO [28,29] for the DFT calculations, and QMCPACK [30] for the QMC calculations. The disordered calculations have been automated using the NEXUS suite of tools [31]. More computational details will be described elsewhere [32].

Finally, theoretical CPs were convoluted by the broadening function due to the instrumental resolution and the final-state effect. The former was monitored by a line profile of the elastic scattering [Fig. 1(b)], which had a width of 0.016 a.u. For the latter, we calculated a spectral density function (SDF) for HEG based on Soininnen's form [22]. The SDF consists of the main feature having a width of ∼0.013 a.u. and a small satellite associated with a plasmon excitation. The broadening function given by a convolution of those functions showed a shape between Gaussian and Lorentzian. We fit this profile with a broadening function $b(p) = 1/[\Sigma_{n=0}^{2} a_n (2p/\Gamma)^{2n}]$ and obtained $(a_0, a_1, a_2) = (1.0, 0.85, 0.15)$ with $\Gamma = 0.024$ a.u. [Fig. 1(d)]. Note this function becomes Lorentzian using the parameters (1, 1, 0) while effectively Gaussian using the parameters (0.6, 0.3, 0.1).

III. RESULTS AND DISCUSSIONS

Figures 2(a) and 2(b) compare the experimental valence CPs $J(p)$ to (convoluted) theory while Figs. 2(c) and 2(d) the experimental $n(k)$ to theory with and without convolutions. As a reference, another $n(k)$ convoluted by Lorentzian having longer tails is also shown. We first computed $J(p)$ with Eq. (1), then convoluted, and finally transformed back to $n(k)$ with Eq. (2). The $n(k)$ of the liquid and solid Li are similar and clear features of the momentum distribution renormalization can be seen. Theory seems to match the experiment better with the Lorentzian-type broadening function, especially the height of $n(k)$ and the curvature near k_F, perhaps implying that SDF could have a larger tail than expected. This possibility will be discussed later. Liquid Li has a slightly lower density, thus a smaller k_F, making $J(p)$ higher for $k < k_F$. Furthermore, $n(k)$ in the liquid shows a slightly smaller drop at k_F possibly because of more disorder effect and larger electron correlation effect in the expanded system. As mentioned above, solid Li has an anisotropic Fermi surface; its radius varies by several percent depending on the directions [13,14]. Hence a simple comparison is problematic. Nonetheless, the comparison across the melting point is consistent with expectations, indicating that the solid sample consists of randomly oriented domains. A sharp drop at k_F persists even after the spherical averaging, as we verified with band theory calculations based on the LDA [see inset in Fig. 2(d)].

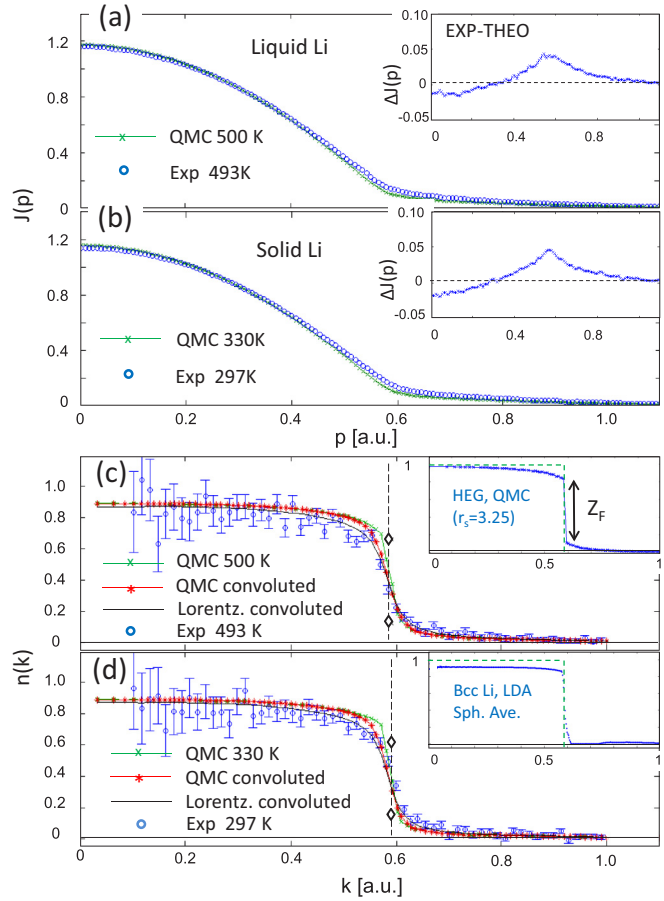

FIG. 2. Valance CPs of liquid (a) and solid Li (b), compared with theory convoluted by the broadening function. The insets show the difference between the experimental and theoretical CPs. EMDs in liquid (c) and solid Li (d), compared to theory with or without the convolutions. The insets show EMD for HEG and the spherically averaged EMD from band theory (LDA). The ◊'s in (c) and (d) show the $n(k_F)$ obtained by RPA fits near k_F.

Z_{k_F} is defined in the limit of $k \to k_F$. Therefore a model to extrapolate $n(k)$ is required to obtain Z_{k_F}. Schülke *et al.* constructed a model where $n(k)$ decreases as $-(k/k_F)^8$ or $(k/k_F)^{-8}$ with increasing k [13]. The $(k/k_F)^{-8}$ behavior is theoretically justified at the limit of large k while it is not otherwise as mentioned in their report. Thus, we adopt a more general power-law model to examine the asymptotic behavior:

$$n(k) = n_0 - \alpha^{-}(k/k_F)^{\beta^{-}} \quad (k \leqslant k_F)$$
$$= \alpha^{+}(k/k_F)^{\beta^{+}} \quad (k > k_F). \tag{3}$$

The − (or +) sign represents the extrapolation from below (or above) k_F.

Figure 3 shows the log-log plots for $n(k)$ vs (k/k_F). Table I summarizes the fit results. We find that the theoretical $n(k)$ has exponents $\beta \sim \pm 4$, depending on the broadening functions. The HEG would have $\beta = -8$ at $k \gg k_F$, which is very different from the results for Li. The reasons for the difference are (i) that HEG can have a different behavior as k approaches k_F and (ii) that *umklapp* process may significantly influence the asymptotic behavior. The experiments, on the other hand,

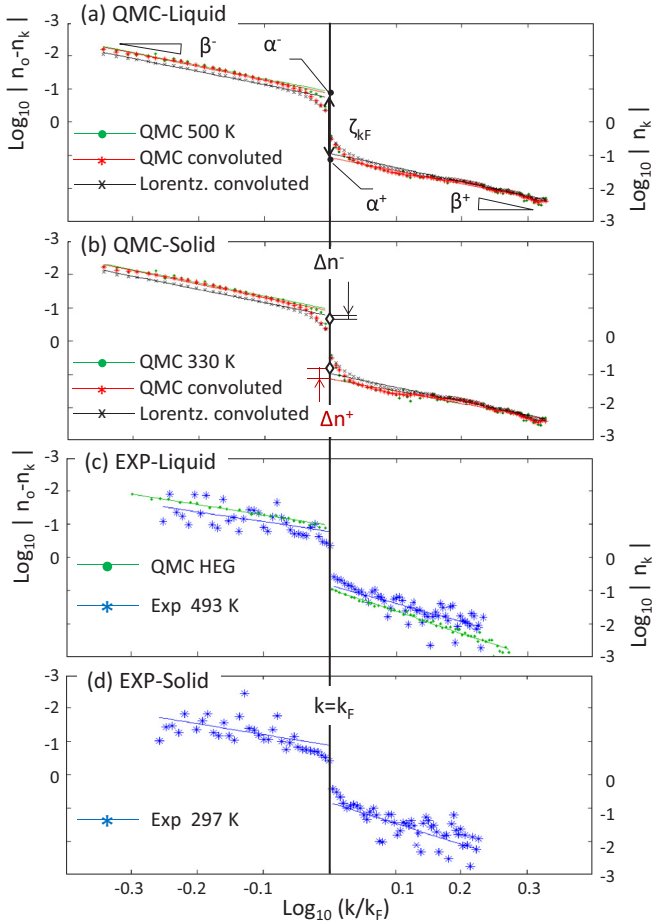

FIG. 3. Momentum densities vs wave vector: Theories for liquid (a) and solid (b) are shown. [·] indicates original outputs (QMC), [∗] convoluted theory (-C), and [×] convoluted with Lorentzian (-CL). Experiments on liquid and solid are shown in (c) and (d). Those for HEG is also shown in (c). ♢ in (b) indicate $n^{\pm}$ by RPA fit ($n^{\pm}_{\rm RPA}$) while $\Delta n^{\pm}$ represents $|n^{\pm}_{\rm pow} - n^{\pm}_{\rm RPA}|$, where $n^{\pm}_{\rm pow}$s are given by power fits for three cases, QMC, QMC-C, and QMC-CL.

show $\beta^+ \sim 3$ and $\beta^- \sim -5$. The difference between theory and experiment may be due to *umklapp* features that appear more prominent in theory. The extrapolated densities α^- and α^+ give $n_o - n^-$ and n^+, respectively. Z_{k_F} is given by $\zeta_{k_F}(n^{\rm FFG}_{k_F}/n^{\rm DFT}_{k_F})$, where $\zeta_{k_F} = n^- - n^+$. We adopt $n^{\rm FFG}_{k_F} = 1$ in free Fermi gas while $n^{\rm DFT}_{k_F} = 0.83$ in LDA band theory. The renormalization factors Z_{k_F} are summarized in Table II.

The power model fits given as Eq. (3) tend to overestimate Z_{k_F} because the momentum distribution is expected to have a divergent slope at k_F [33]. This effect is significant in Li though such a deviation is much smaller in HEG [see Fig. 3(c)]. To account for the slope, we fit the QMC $n(k)$ to the RPA form Eq. (4),

$$\tilde{n}(x) = n_1 + A|1-x|\log(|1-x|), \qquad (4)$$

where $x \equiv k/k_F$, $\tilde{n} \in [0, 1]$. n_1 and A are fitting parameters. The fitted n_1 corresponds to n^- in the range $x \in (0.8, 0.97)$ and n^+ in the range $x \in (1.02, 1.2)$. Points too close to k_F were excluded because spherical average of anisotropic $n(\boldsymbol{k})$ smears out the Fermi break. k_F of the MD configurations

TABLE I. Outputs from "power fit" or linear fit to $\log n(k)$ vs $\log(|k - k_F|)$ plot: Superscripts (a)–(d) indicate correspondences to Figs. 3(a)–3(d).

Theory		α^-	β^-	n_o	α^+	β^+
	QMC	0.145	4.20	0.89	0.091	−4.19
Liquid [(a)]	QMC-C	0.159	4.14	0.89	0.091	−4.20
	QMC-CL	0.204	4.00	0.87	0.120	−4.46
	QMC	0.116	4.99	0.90	0.062	−3.72
Solid [(b)]	QMC-C	0.143	5.35	0.90	0.065	−3.85
	QMC-CL	0.188	4.66	0.88	0.097	−4.28
HEG [(c)]	QMC	0.111	3.13	0.97	0.111	−6.61
Exp.						
Liquid [(c)]		0.169	2.95	0.85	0.142	−5.39
Solid [(d)]		0.134	3.24	0.85	0.144	−6.21

were determined by unfolding the LDA bands from the 432-atom supercell to the primitive cell Brillouin zone using the BANDUP code [34,35]. $Z_{k_F} = \langle \zeta_{k_F} \rangle / n^{\rm LDA}_{k_F}$, where $\langle \cdots \rangle$ indicates average over MD configurations and $n^{\rm LDA}_{k_F} \approx 0.83$. The QMC Z_{k_F} obtained in this way are 0.64 ± 0.01 and 0.54 ± 0.01 for the solid and liquid, respectively. Further, we expect the addition of back flow correlation will reduce QMC Z_{k_F} by ∼5% [26].

The RPA form Eq. (4) cannot be directly fit to the experimental data because of the resolution and final-state smearing

TABLE II. Z_{k_F} and related parameters: Power fit results are from a linear fit to $\log n(k)$ vs $\log(|k - k_F|)$. RPA fit means $n(k)$ is fitted to RPA form Eq. (4). RPA correction applies the correction $n^{\pm}_{\rm cor} = n^{\pm}_{\rm pow}$(Exp.)$+\Delta n^{\pm}$, where $\Delta n^{\pm} = n^{\pm}_{\rm RPA}$(Theo.)$-n^{\pm}_{\rm pow}$(Theo.). Theory QMC are the raw QMC $n(k)$ values, QMC-C values are corrected with the optimally fit convolution, and QMC-CL are from the Lorentzian convolution having long tails. The bold values are our best estimates.

Power fit			$n^-_{\rm pow}$	$n^+_{\rm pow}$	ζ_{k_F}	Z_{k_F}
	Theo.	QMC	0.74	0.091	0.65	0.78
Liquid		QMC-C	0.73	0.091	0.64	0.77
		QMC-CL	0.67	0.120	0.55	0.66
	Exp.		0.69	0.142	0.54	0.62
	Theo.	QMC	0.75	0.082	0.67	0.81
Solid		QMC-C	0.74	0.084	0.66	0.80
		QMC-CL	0.68	0.113	0.57	0.68
	Exp.		0.72	0.144	0.57	0.65
RPA fit			$n^-_{\rm RPA}$	$n^+_{\rm RPA}$		
Liquid	Theo.	QMC	0.61	0.155	0.45	**0.54**
Solid	Theo.	QMC	0.66	0.125	0.53	**0.64**
RPA correction			$n^-_{\rm cor}$	$n^+_{\rm cor}$		
	Exp.	QMC	0.56	0.206	0.35	0.42
Liquid		QMC-C	0.57	0.206	0.36	**0.43**
		QMC-CL	0.63	0.178	0.45	0.54
	Exp.	QMC	0.62	0.187	0.44	0.53
Solid		QMC-C	0.63	0.185	0.45	**0.54**
		QMC-CL	0.69	0.156	0.54	0.65

effects at k_F. Therefore, we use theory to determine the slope near k_F and attempt to correct the experimental ζ_{k_F} and Z_{k_F}. The difference between the extrapolated densities in the two models $\Delta n^{\pm} = n^{\pm}_{\mathrm{RPA}}(\mathrm{Theo.}) - n^{\pm}_{\mathrm{pow}}(\mathrm{Theo.})$ are used for the corrections to the experiments. $\Delta n^{\pm}$ depends on a shape of the broadening function $b(p)$, which involves the SDF. The shape is not exactly known (see Table II) and it leads to an uncertainly for determining Z_{k_F}. Experimental values for $n^{\pm}$, ζ_{k_F}, and Z_{k_F} after the corrections are shown in Table II. Assuming the behavior of the QMC determined $n(k)$ for k near k_F, an upper estimate for experimental Z_{k_F} is 0.54 (liquid) and 0.65 (solid) by the broadest, Lorentzian-type $b(p)$ while the lower estimates are 0.42 (liquid) and 0.53 (solid) by the narrowest $b(p)$.

IV. CONCLUSION

In summary, we obtained in experiment $Z_{k_F} = 0.43^{+0.11}_{-0.01}$ for liquid Li and $0.54^{+0.11}_{-0.02}$ for solid Li, while using QMC we obtained 0.54 ± 0.01 for the liquid and 0.64 ± 0.01 for the solid. The agreement is much better than in previous studies. To reduce the experimental errors further, the broadening due to final state effects needs to be made smaller. It is possible if Compton scattering is performed at higher energies, e.g., at $\geqslant$50 keV while keeping an instrumental resolution of $\sim$0.01 a.u. Such an experiment is a technical challenge at present but we believe it will be available in the near future since the synchrotron radiation techniques are being advanced day to day.

ACKNOWLEDGMENTS

The experiment was performed under approvals of SPring-8 (Proposals 2011B4250, 2012A4253, -4254) and National Synchrotron Radiation Research Center, Taiwan (2011-2-105). D.C. and Y.Y. were supported by DOE Grant No. NA DE-NA0001789. This work made use of the Blue Waters sustained-petascale computing project and the Illinois Campus Cluster, supported by the National Science Foundation (Awards No. OCI-0725070 and No. ACI-1238993), the state of Illinois, the University of Illinois at Urbana-Champaign and its National Center for Supercomputing Applications.

[1] P. Nozières, *Theory of Interacting Fermi Systems: Chapter 4* (Westview Press, Colorado, 1964).
[2] G. D. Mahan, *Many Particle Physics: Chapter 5* (Kluwer Academic/Plenum Publishers, New York, 1981).
[3] G. F. Giuliani and G. Vignale, *Quantum Theory of The Electron Liquid: Chapter 8* (Cambridge University Press, Cambridge, 2005).
[4] M. Holzmann, B. Bernu, C. Pierleoni, J. McMinis, D. M. Ceperley, V. Olevano, and L. Delle Site, Phys. Rev. Lett. **107**, 110402 (2011).
[5] H. Maebashi and Y. Takada, Phys. Rev. B **84**, 245134 (2011).
[6] J. Otsuki, H. Kusunose, and Y. Kuramoto, Phys. Rev. Lett. **102**, 017202 (2009).
[7] E. Eidelstein, S. Moukouri, and A. Schiller, Phys. Rev. B **84**, 014413 (2011).
[8] S. Sykora and K. W. Becker, Phys. Rev. B **98**, 245139 (2018).
[9] W. Schülke, *Electron Dynamics by Inelastic X-ray Scattering: Chapter 4* (Oxford University Press, Oxford, 2007).
[10] P. Eisenberger and P. M. Platzman, Phys. Rev. A **2**, 415 (1970).
[11] I. G. Kaplan, B. Barbiellini, and A. Bansil, Phys. Rev. B **68**, 235104 (2003).
[12] S. Huotari, J. A. Soininen, T. Pylkkänen, K. Hämäläinen, A. Issolah, A. Titov, J. McMinis, J. Kim, K. Esler, D. M. Ceperley *et al.*, Phys. Rev. Lett. **105**, 086403 (2010).
[13] W. Schülke, G. Stutz, F. Wohlert, and A. Kaprolat, Phys. Rev. B **54**, 14381 (1996).
[14] Y. Sakurai, Y. Tanaka, A. Bansil, S. Kaprzyk, A. T. Stewart, Y. Nagashima, T. Hyodo, S. Nanao, H. Kawata, and N. Shiotani, Phys. Rev. Lett. **74**, 2252 (1995).
[15] Y. Kubo, J. Phys. Soc. Jpn. **65**, 16 (1996).
[16] Y. Kubo, J. Phys. Soc. Jpn. **66**, 2236 (1997).
[17] C. Filippi and D. M. Ceperley, Phys. Rev. B **59**, 7907 (1999).
[18] S. B. Dugdale and T. Jarlborg, Solid State Commun. **105**, 283 (1998).
[19] C. Sternemann, T. Buslaps, A. Shukla, P. Suortti, G. Döring, and W. Schülke, Phys. Rev. B **63**, 094301 (2001).
[20] E. Klevak, F. D. Vila, J. J. Kas, J. J. Rehr, and G. T. Seidler, Phys. Rev. B **94**, 214201 (2016).
[21] C. Sternemann, K. Hämäläinen, A. Kaprolat, A. Soininen, G. Döring, C. C. Kao, S. Manninen, and W. Schülke, Phys. Rev. B **62**, R7687(R) (2000).
[22] J. A. Soininen, K. Hämäläinen, and S. Manninen, Phys. Rev. B **64**, 125116 (2001).
[23] N. Hiraoka, H. Fukui, H. Tanida, H. Toyokawa, Y. Q. Cai, and K.-D. Tsuei, J. Synchrotron Radiat. **20**, 266 (2013).
[24] P. Fajardo, V. Honkimäki, T. Buslaps, and P. Suortti, Nucl. Instrum. Methods Phys. Res., Sect. B **134**, 337 (1998).
[25] C. Filippi and D. M. Ceperley, Phys. Rev. B **57**, 252 (1998).
[26] M. Holzmann, B. Bernu, V. Olevano, R. M. Martin, and D. M. Ceperley, Phys. Rev. B **79**, 041308(R) (2009).
[27] S. Plimpton, J. Comput. Phys. **117**, 1 (1995).
[28] P. Giannozzi, S. Baroni, N. Bonini, M. Calandra, R. Car, C. Cavazzoni, D. Ceresoli, G. L. Chiarotti, M. Cococcioni, I. Dabo *et al.*, J. Phys.: Condens. Matter **21**, 395502 (2009).
[29] P. Giannozzi, O. Andreussi, T. Brumme, O. Bunau, M. B. Nardelli, M. Calandra, R. Car, C. Cavazzoni, D. Ceresoli, M. Cococcioni *et al.*, J. Phys.: Condens. Matter **29**, 465901 (2017).
[30] J. Kim, A. D. Baczewski, T. D. Beaudet, A. Benali, M. C. Bennett, M. A. Berrill, N. S. Blunt, E. J. L. Borda, M. Casula, D. M. Ceperley *et al.*, J. Phys.: Condens. Matter **30**, 195901 (2018).
[31] J. T. Krogel, Comput. Phys. Commun. **198**, 154 (2016).
[32] Y. Yang, N. Hiraoka, K. Matsuda, M. Holzmann, and D. M. Ceperley, Phys. Rev. B **101**, 165125 (2020).
[33] P. Gori-Giorgi and P. Ziesche, Phys. Rev. B **66**, 235116 (2002).
[34] P. V. C. Medeiros, S. Stafström, and J. Björk, Phys. Rev. B **89**, 041407(R) (2014).
[35] P. V. C. Medeiros, S. S. Tsirkin, S. Stafström, and J. Björk, Phys. Rev. B **91**, 041116(R) (2015).